



## Research Paper

Biodiesel production from used cooking oil using a novel surface functionalised TiO<sub>2</sub> nano-catalystJabbar Gardy<sup>a</sup>, Ali Hassanpour<sup>a,\*</sup>, Xiaojun Lai<sup>a</sup>, Mukhtar H. Ahmed<sup>b</sup>, Mohammad Rehan<sup>c</sup><sup>a</sup> School of Chemical and Process Engineering, University of Leeds, LS2 9JT Leeds, UK<sup>b</sup> Nanotechnology Integrated Bioengineering Centre, University of Ulster, Jordanstown, BT37 0QB Belfast, UK<sup>c</sup> Centre of Excellence in Environmental Studies (CEES), King Abdulaziz University, Jeddah, Saudi Arabia

## ARTICLE INFO

## Article history:

Received 29 November 2016

Received in revised form 11 January 2017

Accepted 28 January 2017

Available online 4 February 2017

## Keywords:

TiO<sub>2</sub>/propyl sulfonic acid  
 Solid acid nano-catalyst  
 Esterification and transesterification  
 Biodiesel  
 Used cooking oil

## ABSTRACT

A novel, efficient and recyclable mesoporous TiO<sub>2</sub>/PrSO<sub>3</sub>H solid acid nano-catalyst was synthesised by the post-synthetic grafting of propyl sulfonic acid groups onto a mixed phase of a TiO<sub>2</sub> support. The synthesised nano-catalyst was characterised using FTIR, SEM, TEM, XPS, N<sub>2</sub> adsorption–desorption isotherms, XRD, DSC, TGA, and CHNS analysis. The loading percentage of propyl sulfonic acid on the TiO<sub>2</sub> support was calculated using CHNS analysis and TGA. The catalytic performance of TiO<sub>2</sub>/PrSO<sub>3</sub>H on the production of the fatty acid methyl esters (FAME) via simultaneous esterification and transesterification reactions from used cooking oil (UCO) has been studied. The effects of different process parameters showed that 98.3% of FAME can be obtained after 9 h of reaction time with 1:15 molar ratio of oil to methanol, 60 °C reaction temperature and 4.5 wt% catalyst loading. It was also found that the one-pot post-surface functionalisation strategy with hydrophilic functional groups (–SO<sub>3</sub>H) enhanced the acid strengths of the nano-catalyst providing more acid sites for the reactants, and improving the accessibility of methanol to the triglycerides (TG)/free fatty acids (FFAs) by increasing the pore volumes/sizes of the nano-catalyst. The solid acid nano-catalyst was re-used in four consecutive runs without significant loss of catalytic efficiency. Finally, the synthesised biodiesel fuel satisfied ASTM and EN standards.

© 2017 Elsevier B.V. All rights reserved.

## 1. Introduction

Nanomaterials have fascinating and unique properties for the usage in various industrial fields. Titanium dioxide nanoparticles (TiO<sub>2</sub> NPs) are among the most widely studied for their use in photocatalysis, gas sensors, medicine, catalyst support, pigments, cosmetics and solar cells [1–3]. This is due mainly to their favourable properties, acidity, wide band gap, high surface area, low cost and high availability, better redox selectivity, good mechanical and chemical stability, high reactivity, low toxicity, and high reusability [4–6]. TiO<sub>2</sub> NPs naturally occur in three main crystallographic phases, these being anatase, rutile, and brookite [2], but the most commonly used, because of its highly photocatalytic activity properties, is a mixture of anatase and rutile phases of TiO<sub>2</sub> [7].

Because of their multiple potential applications, straightforward recoverability and excellent properties, a wide range of recent studies on synthetic routes have been undertaken to fabricate surface

modified nanoparticles in order to increase their surface acidity/basicity [8–13]. This is of particular significance in relation to nano-catalysts for biodiesel production involving the use of cheap raw materials containing FFAs as the acid catalysts can facilitate simultaneous esterification of FFAs and transesterification of TG without soap formation [14,15]. In the context of green chemistry, recycled vegetable oils could be used as inexpensive feedstocks for biodiesel fuel production [16–18]. Such use helps to reduce environmental pollution and utilises economies for cheap biodiesel production [19–21]. The yield and quality of biodiesel can be highly affected by the surface area, surface acidity/basicity, and particle size of the catalysts used in the esterification and/or transesterification processes [22]. This has encouraged the development of novel recyclable solid acid nano-catalysts to replace conventional corrosive homogeneous acid catalysts [21,23], which can corrode reactors and requires further washing with neutralisation steps for their removal from the biodiesel and its by-products [24].

According to the literature, the surface modification of nanoparticles could create solid acid nano-catalysts [25]. The surface modification could be carried out through different strategies such as chemical treatments, ozonolysis, polymer grafting,

\* Corresponding author. Tel.: +44 1133432405.

E-mail address: [a.hassanpour@leeds.ac.uk](mailto:a.hassanpour@leeds.ac.uk) (A. Hassanpour).

encapsulation in a silica shell (silanisation), ligand exchange technique, or capping agents (surfactants)/encapsulation in a surfactant corona [26,27]. Modification of the surface of nanoparticles by integration of acidic functional groups (e.g.  $-\text{SO}_3\text{H}$ ) to produce solid acid catalysts for different applications has been highlighted in the literature over the recent years [8,11,21,24,28–38]. This is because sulfonic acid functional groups on the surface of nanoparticles lead to the formation of porous materials with high accessibility to the active sites [39].

There are several recent works describing the performance of such promising materials for the biodiesel production [10,19,31,40–42]. The surface modification of mesoporous materials, such as SBA-15, with organosilane sulfonic groups increases the hydrophobic character of the solid acid catalyst surface resulting in high catalytic activity and selectivity toward glycerol in the esterification of FFAs [43]. However, these types of catalysts are quite sensitive to the presence of impurities in raw materials such as recycled oil feedstocks [44]; also, low sulfonic acid sites loading on the surface of nanoparticles are hampered in practical application of such catalysts [37]. Furthermore, fast deactivation is another practical problem for such catalyst. Therefore, there is a need to synthesise stronger and more tolerant nano-catalysts with higher re-usability for cheap feedstocks such as used cooking oil (UCO).

There are, so far, no reports on the surface functionalisation of titania with 1,3-propyl sultone for a direct-preparation of propyl-sulfonic acid grafting the surface of  $\text{TiO}_2$  NPs and/or on the use of such material as a solid acid nano-catalyst for biodiesel production. Therefore, the present work describes the fabrication, characterisation and application of a novel  $\text{TiO}_2$ /propylsulfonic acid nano-catalyst in order to understand the impact of catalytic activity and reusability of such nano-catalyst on biodiesel production from UCO as a cheap feedstock. Finally, the synthesised biodiesel from the catalytic esterification/transesterification processes was analysed in accordance to ASTM and EN standard methods.

## 2. Experimental

### 2.1. Materials and methods

#### 2.1.1. Synthesis of solid acid nano-catalysts

The surface charge of titania NPs is pH dependent. Therefore, we pre-treated the titania NPs with aqueous solution of ammonium hydroxide to reduce the agglomeration and increase the receptor sites ( $\text{TiO}_2 + \text{NOH}^- \rightarrow \text{TiO}_2(\text{OH})^{\text{n}^-}$ ) on the surface of titania support [45]. 6 g of  $\text{TiO}_2$  NPs (Sigma-Aldrich) was added slowly into a 50 ml of 0.5 M ammonium hydroxide solution (Sigma-Aldrich) at room temperature. The suspension was then sonicated for 30 min. The resultant was transferred into a centrifuge tube for washing with double deionised water and dried at 80 °C for 4 h in an oven. Typically, 1 g of the dried powder was charged into a three necked glass flask at ambient temperature then 20 ml suspension solutions of 0.1 molar 1,3-propane sulfone (Sigma-Aldrich) in dry toluene (Sigma-Aldrich) was added dropwise. The resultant suspension was slowly stirred under reflux for 72 h at 120 °C. The synthesised  $\text{TiO}_2$ /propyl sulfonic acid powders were cooled to room temperature. Thereafter the synthesised nano-catalyst was separated from the solution using a centrifuge and washed off several times with fresh toluene to remove the remained unreacted 1,3-propane sulfone. The resulting precipitate sample was dried overnight at 80 °C then denoted as  $\text{TiO}_2/\text{PrSO}_3\text{H}$ .

#### 2.1.2. Synthesis of biodiesel fuel

The simultaneous esterification and transesterification of UCO was performed in a glass batch reactor connected with an automatic temperature controller loop system under constant agitation rate at

600 RPM using a digital mechanical stirrer and a reflux condenser. The sample of UCO obtained from a local restaurant in Leeds, UK, was pre-treated by filtration process to remove solid impurities and heated to 100 °C for a few hours to remove the moistures. Specified amounts of pre-treated UCO,  $\text{TiO}_2/\text{PrSO}_3\text{H}$  nano-catalyst and methanol (Sigma-Aldrich) were charged into the batch reactor. The three-phase (solid–liquid–liquid) mixture was mixed at 600 RPM and heated to specified temperatures and times. The final reaction mixture was transferred into a separating funnel and allowed to cool to room temperature. A few millilitres of aliquot was withdrawn from the upper layer, biodiesel phase, and separated from the remaining impurities using a centrifuge at 9000 RPM for 10 min to quantify the fatty acid methyl ester (FAME) content of the samples by off-line gas chromatography (GC) [4].

### 2.2. Characterisation methods

#### 2.2.1. Catalyst characterisation

Physicochemical properties of the prepared  $\text{TiO}_2/\text{PrSO}_3\text{H}$  and  $\text{TiO}_2$  nano-catalysts were fully characterised as follows: Fourier transform infrared (FT-IR) spectroscopy was measured at room temperature using a Nicolet iS10 FT-IR spectrometer fitted with a DTGS-KBr detector. A minimum of 36 scans were performed at the average signal of infrared with a resolution  $4\text{ cm}^{-1}$  in the ranges of 500 to  $4000\text{ cm}^{-1}$ . Particle size and surface morphologies were observed with a high performance cold field emission scanning electron microscopy (CFE-SEM, SU8230 Hitachi) and transmission electron microscopy (TEM, FEI Titan Themis Cubed 300). The location of the elements and elemental compositions of the prepared nano-catalyst sample were identified using the TEM fitted with high-angle annular dark field (HAADF) detector operated at an accelerating voltage of 300 kV equipped with an energy dispersive X-ray spectroscopy (EDS, Oxford INCA 350). Nitrogen porosimetry was obtained at  $-196\text{ }^\circ\text{C}$  on a Micromeritics TriStar 3000 surface analyser. Prior to the measurements, the nano-catalyst sample was degassed in a vacuum oven overnight at  $120\text{ }^\circ\text{C}$ . The X-ray photoelectron spectroscopy (XPS) was performed using a KRATOS XSAM 800 equipped with an energy analyser and monochromated Al-K $\alpha$  X-ray source ( $\text{hv}1486\text{ eV}$ ) generated from aluminium anode. The film of the nano-catalyst sample was prepared by dissolving a few milligrams of catalyst sample in chloroform and methanol (3:1) then coating on the silicon wafer surface. CasaXPS version 2.3.17 was used for spectral fitting and binding energies corrected to the C 1s peak at 285 eV to compensate for residual charging effects. The bulk and surface sulfonic acid loadings on the surface of the nano-catalysts were determined via elemental analysis (Thermo Scientific™ FLASH 2000 CHNS Analyser) and XPS, respectively. The thermal stability was carried out on a Mettler Toledo (TGA/DSC-1) star<sup>e</sup> system. The system was programmed to heat up from 25 to  $900\text{ }^\circ\text{C}$  at  $10\text{ }^\circ\text{C}/\text{min}$  under nitrogen gas at 50 ml/min with a constant flow rate. Total propyl sulfonic acid loadings were calculated from the TGA weight loss between 200 and  $600\text{ }^\circ\text{C}$ . XRD patterns were recorded on a Bruker D8 X-ray diffraction, fitted with a Cu K $\alpha$  radiation ( $1.54\text{ \AA}$ , 40 kV, 40 mA). Data was collected from  $2\theta$  angle ranging of  $10\text{--}70\text{ }^\circ$  with step size  $0.0495\text{ }^\circ$  at 35 s per step.

#### 2.2.2. Biodiesel characterisation

The flash point of prepared biodiesel sample was measured by an auto ramp closed cup flash point tester (Setaflash series 3, England) equipped with a coolant block unit. The temperature ramped at  $1\text{--}2\text{ }^\circ\text{C}/\text{min}$  until the flash was captured. Moreover, the pycnometric method was used to determine the density of obtained biodiesel at  $15\text{ }^\circ\text{C}$ . Furthermore, viscosity of prepared biodiesel was measured on a Bohlin-Gemini 150 rotary rheometer (Malvern, UK). Additionally, trace moisture content in biodiesel was analysed by volumetric Karl Fischer titration (Mettler Toledo-V20, Germany).

The acid values and percentage of FFA were measured according to the standard methods [4]. The cloud point of prepared biodiesel was examined by a differential scanning calorimetry (DSC 1, Mettler Toledo, UK) equipped with an intracooler system (Huber TC45). (5±2.5) mg of biodiesel sample was accurately weighted in a 40 µl sealed standard aluminium pan and placed in the DSC sample chamber. The experiment was initiated by keeping the sealed sample pan at 50 °C for 5 min to homogenise the sample should it contain any wax materials. The system was then cooled to –30 °C at 1 °C/min and held at that temperature for 5 min. The sealed sample pan was then heated to 50 °C at 1 °C/min and held at that temperature for 5 min. Nitrogen gas, at a constant flow rate of 50 ml/min, was used as a purge gas during all steps in this experiment and analysed using Mettler Star<sup>e</sup> software. The cloud point was the onset temperature of the initial exothermic peak on the cooling curve. Finally, the thermal stability of prepared biodiesel was assessed on the Stanton Redcroft thermogravimetric analysis (TGA-TGH 1000) on 20–25 mg of biodiesel sample at 10 °C/min during heating from 25 to 700 °C under air gas at 50 ml/min with a constant flow rate.

### 3. Results and discussion

#### 3.1. Catalyst characterisation

TiO<sub>2</sub>/PrSO<sub>3</sub>H nano-catalyst was prepared by the reaction of TiO<sub>2</sub> NPs support with an extremely reactive sulfoalkylating agent to increase the surface acidity of TiO<sub>2</sub> NPs. The concentration of propyl sulfonic acid groups attached on the surface of TiO<sub>2</sub> NPs mainly depends on the amount of available –O-H terminated adsorption sites. Such surface modification was formed through a ring opening reaction of 1,3-propane sultone with nucleophile cleaving the carbon-oxygen bond as shown in proposed Scheme 1.

Fig. 1 illustrates the FT-IR spectra over the range 500–4000 cm<sup>-1</sup>, corresponding to the TiO<sub>2</sub> (in red) and TiO<sub>2</sub>/PrSO<sub>3</sub>H (in black) nano-catalysts. The FT-IR spectrum for TiO<sub>2</sub>/PrSO<sub>3</sub>H nano-catalyst shows several extra peaks compared to TiO<sub>2</sub> NPs spectrum. The broad band in the range of 500–626.4 cm<sup>-1</sup> assigned to Ti-O stretching vibrations can be clearly observed in both spectra [46]. The appearance of a new strong peak at 1031 cm<sup>-1</sup> assigned to the stretching vibration of S-O bond, whereas the band occurring at 1130 cm<sup>-1</sup> corresponded to C-O stretching vibration [47]. Moreover, the existed band at 1198 cm<sup>-1</sup> attributed to the C-C stretching vibration. The new extra two peaks appeared on the black spectrum at around 1275 and 1362.5 cm<sup>-1</sup> are considered to be a fingerprint of the S=O symmetric and asymmetric stretching vibrations, respectively, for sulfonic acid groups attachment on the surface of TiO<sub>2</sub> NPs [47]. Similarly, the new peaks located at 1416 and 1447 cm<sup>-1</sup> are attributed to the methylene groups [-CH<sub>2</sub>-] bending in PrSO<sub>3</sub>H functional groups [47]. The region below 3000 cm<sup>-1</sup> clearly showed two distinct peaks at 2886 and 2946 cm<sup>-1</sup> that are likely to represent the C-H stretching vibrations, representing symmetric and asymmetric modes respectively, for the -CH<sub>2</sub>- groups in PrSO<sub>3</sub>H functional groups [47,48].

Furthermore, the weak absorption bands at 1640 cm<sup>-1</sup> in TiO<sub>2</sub> NPs and 1712 cm<sup>-1</sup> in TiO<sub>2</sub>/PrSO<sub>3</sub>H belong to H–O–H symmetric vibration of the physisorbed water molecules on the surface. Whilst the region between 1975 and 2160 cm<sup>-1</sup> clearly showed few peaks related to the asymmetric stretching of CO<sub>2</sub> molecules adsorbed on the surface of both TiO<sub>2</sub>/PrSO<sub>3</sub>H and TiO<sub>2</sub> nano-catalysts [4,49]. Additionally, the broad band at 3200–3500 cm<sup>-1</sup> in TiO<sub>2</sub>/PrSO<sub>3</sub>H nano-catalyst assigned to O–H stretching vibration of sulfonic acid functional groups on the surface of TiO<sub>2</sub>-NPs [47].

Surface morphological and structure features of the TiO<sub>2</sub> NPs and TiO<sub>2</sub>/PrSO<sub>3</sub>H nano-catalysts were examined by using Hitachi

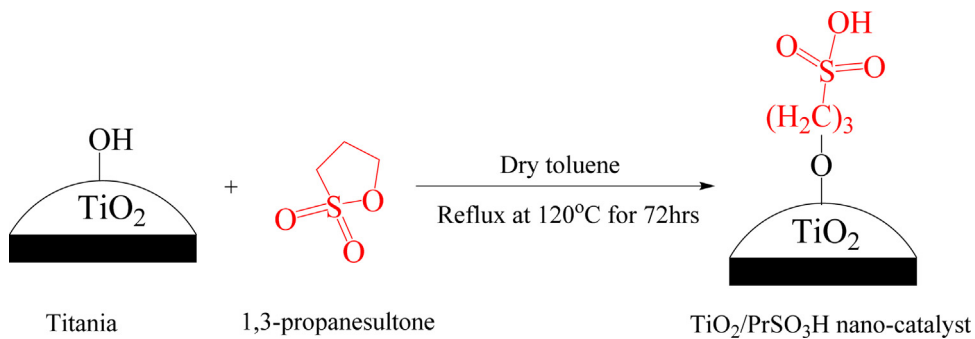
CFE-SEM. It is clear from Fig. 2a that TiO<sub>2</sub>-NPs have relatively uniform sized particles with some agglomerates. Moreover, the TiO<sub>2</sub>-NPs exhibit mainly spherical like morphology distribution. TiO<sub>2</sub>/PrSO<sub>3</sub>H nano-catalyst (see Fig. 2b), however, showed non-uniform particle size distributions with well-defined hexagonal, tetragonal and cubic shaped structures (inset SEM image @ 250 K magnification). This may suggest that the surface modification caused slight enlargement of the particle sizes of TiO<sub>2</sub> support as can be seen clearly in Fig. 2b (inset).

The particle size enlargements and different morphologies for TiO<sub>2</sub>/PrSO<sub>3</sub>H nano-catalyst are also clearly seen in TEM images (Fig. 3). TiO<sub>2</sub>/PrSO<sub>3</sub>H agglomerated resulting in larger clusters owing to interaction between the head groups of PrSO<sub>3</sub>H on the surface of TiO<sub>2</sub>-NPs. It is also important to mention that the enlarged particle sizes (red arrow) of as-synthesised TiO<sub>2</sub>/PrSO<sub>3</sub>H, observed in different TEM images, were due to the effects of surface grafting. The TEM images also show mixture of tetragonal/cubic/hexagonal morphologies of TiO<sub>2</sub>/PrSO<sub>3</sub>H nano-catalyst with good crystallinity. The uniform and narrow particle size distributions of prepared nano-catalyst mainly depend on the initial TiO<sub>2</sub>-NPs support with the grafting of 1,3-propane sultone into the surface of TiO<sub>2</sub> around the particle. A similar case has been reported for surface modification of different particles using silanisation method [50]. The number based particle size distributions of TiO<sub>2</sub>/PrSO<sub>3</sub>H were estimated from different TEM images and presented as histograms in Fig. 4. These particles were found to have size range of 8.2–42 nm with an average particle size of 23.1 nm; whereas, the average particle size of initial TiO<sub>2</sub> NP was 22.34 nm [4].

HRTEM and SAED were used to investigate the particle morphologies as depicted in Fig. 5a and b. As shown from the HRTEM images (Fig. 5a), two different kinds of lattice fringes were observed, which were attributed to [101] interplanar spacing of anatase phase and [200] interplanar spacing of rutile phase with a tiny amorphous layer surrounding the surface of each particle. This indicates that [101] and [200] facets have more preferable planes in anatase and rutile crystal phases, respectively. Noticeably, the d-spacing of the surface grafting nano-catalyst has expanded (inset in Fig. 5a) with good core crystallinity regardless of the presence of PrSO<sub>3</sub>H groups on the surface. Furthermore, several obtained SAED patterns confirm the mixed phases of rutile and anatase with poly-crystallinities, in the TiO<sub>2</sub>/PrSO<sub>3</sub>H nano-catalyst as shown in Fig. 5b. In addition, the clear poly-crystallinity rings/spots correspond to the [101], [116], [004], [200], [220], [213], [216] and [204] lattice planes of anatase TiO<sub>2</sub> crystal phase in TiO<sub>2</sub>/PrSO<sub>3</sub>H nano-catalyst. The other poly-crystallinity rings/spots, on the other hand, attributed to the [101], [210], [220], [310], [110], [200], [111], [202], [410], [221] and [202] lattice spacing of rutile TiO<sub>2</sub> crystal phase in TiO<sub>2</sub>/PrSO<sub>3</sub>H nano-catalyst.

STEM electron energy loss spectroscopy (EELs)-maps for TiO<sub>2</sub>/PrSO<sub>3</sub>H nano-catalyst was performed to obtain more information about the loading of carbon and sulphur layers on the surface of TiO<sub>2</sub> NPs. Titanium, carbon and sulphur maps were extracted from the spectrum imaging high loss region. Fig. 6 demonstrates the high resolution elemental mapping of titanium, carbon and oxygen layer-by-layer distributions onto the TiO<sub>2</sub>/PrSO<sub>3</sub>H particles. It can be observed that the surfaces of TiO<sub>2</sub> NPs are uniformly covered by carbon and sulphur layers. These homogenous distributions of carbon and sulphur clearly confirms the surface of TiO<sub>2</sub> NPs have been functionalised by PrSO<sub>3</sub>H groups. This also explains the reason for surface area reduction (Fig. 7b) and some surface roughness of particles (Fig. 5a). The STEM image further shows clear porous structures between TiO<sub>2</sub>/PrSO<sub>3</sub>H particles.

Nitrogen adsorption-desorption isotherms and pore volume/size distributions of TiO<sub>2</sub> and TiO<sub>2</sub>/PrSO<sub>3</sub>H samples are presented in Fig. 7. The surface area was calculated from the



**Scheme 1.** General proposed protocol for the synthesis of TiO<sub>2</sub>/PrSO<sub>3</sub>H nano-catalyst.

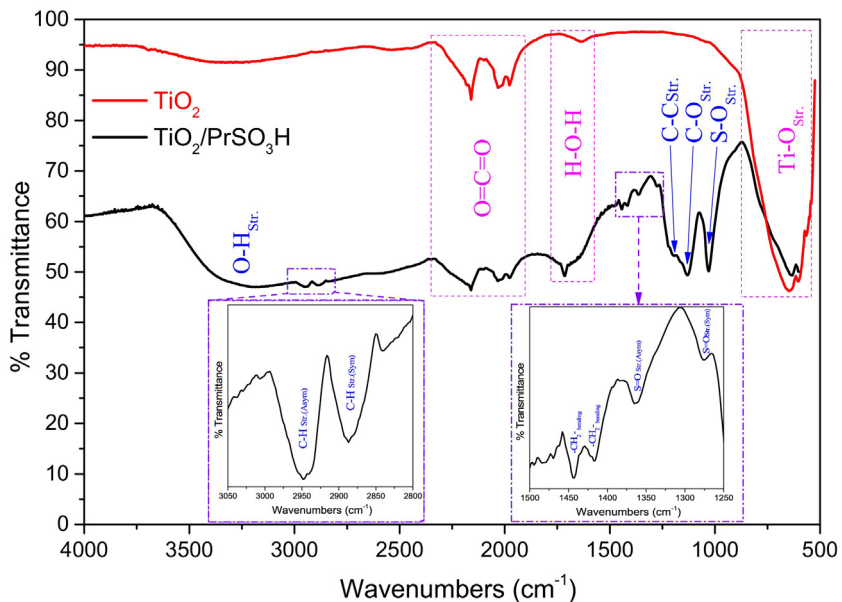


**Fig. 1.** FT-IR spectra of TiO<sub>2</sub>/PrSO<sub>3</sub>H (in black) and TiO<sub>2</sub> (in red) nano-catalysts.

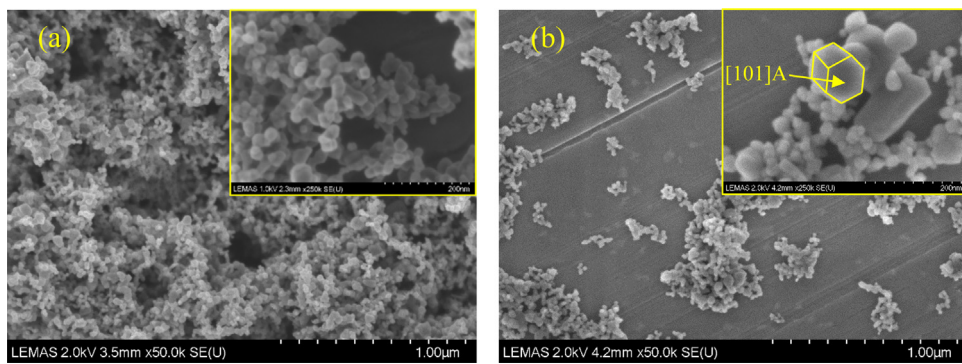


**Fig. 2.** SEM images showing particle size and morphology distributions of (a) TiO<sub>2</sub> and (b) synthesised TiO<sub>2</sub>/PrSO<sub>3</sub>H nano-catalysts.

nitrogen adsorption isotherms using the Brunauer–Emmett–Teller (BET) method, but the mean pore size and total pore volume were calculated from the desorption branch of the isotherm using the Barrett–Joyner–Halenda (BJH) methods. The adsorption isotherms for both catalysts were determined in the range  $P/P_0 = 0.06–0.2$ , wherein a liner relationship was maintained, which revealed that both materials are typical type IV isotherms within mesoporous structure. The differences in condensation and evaporation were attributed to the monolayer-multilayer adsorption according to the IUPAC - behaviour, associated with mesoporous materials. The

hysteresis loop shape for as-synthesised TiO<sub>2</sub>/PrSO<sub>3</sub>H at relative pressure in the range of 0.75–0.985 was classified as H1-type, indicating a capillary condensation in mesoporous structure [51]. It should be noted from Fig. 7 (inset) that the pore volume distributions in TiO<sub>2</sub>/PrSO<sub>3</sub>H nano-catalyst has much larger mesopores with an increase of pore diameter compared with the initial TiO<sub>2</sub> NPs. The large pore size is much more preferable for minimising diffusion limitations for long alkyl chain hydrocarbons in FFA/TG in esterification and transesterification reactions [4,14,52].

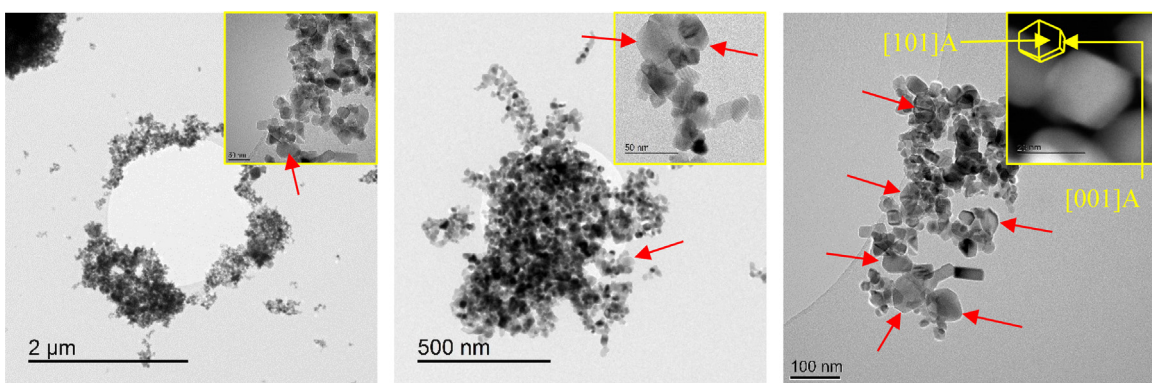


**Fig. 3.** TEM images at different magnifications of synthesised  $\text{TiO}_2/\text{PrSO}_3\text{H}$  nano-catalyst.

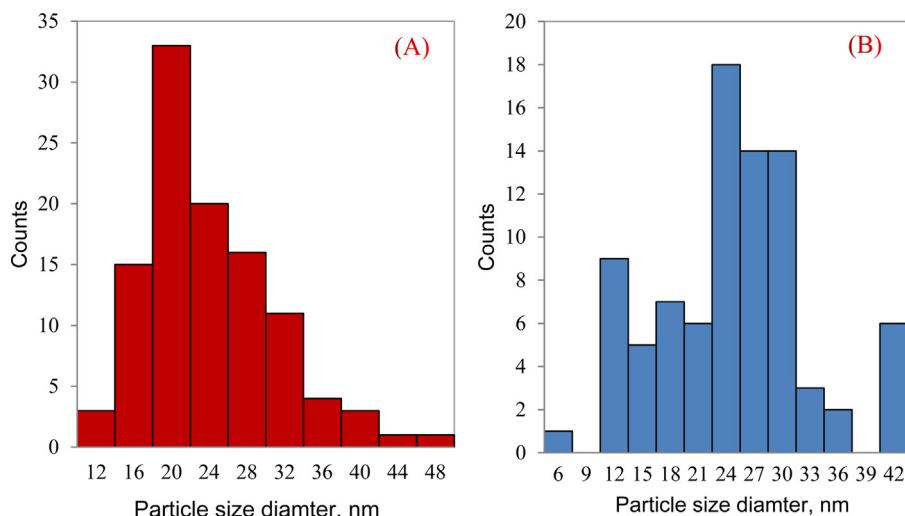


**Fig. 4.** Particle size distributions for (a)  $\text{TiO}_2$  and (b)  $\text{TiO}_2/\text{PrSO}_3\text{H}$  nano-catalysts.

**Table 1**  
Physicochemical parameters of  $\text{TiO}_2/\text{PrSO}_3\text{H}$  nano-catalyst.

	Texture properties <sup>a</sup>			CHNS analysis <sup>b</sup>		TEM-EDS <sup>c</sup>
	$S_{\text{BET}}$	$V_p$	$D_p$	C%	S%	S%
$\text{TiO}_2/\text{PrSO}_3\text{H}$	38.59	0.192	24.55	1.41	0.28	0.26

<sup>a</sup>  $S_{\text{BET}}$ : BET surface area ( $\text{m}^2 \text{ g}^{-1}$ ) calculated over the relative pressure range 0.06–0.2,  $D_p$ : Mean pore size (nm) calculated by applying the BJH model from  $N_2$  desorption isotherm;  $V_p$ : Total pore volume ( $\text{cm}^3 \text{ g}^{-1}$ ) was determined at  $P/P_0 = 0.98$ .

<sup>b</sup> C%: Carbon%, and S%: Sulphur% determined by using elemental (CHNS) analysis.

<sup>c</sup> The overall of sulphur loading on the surface of  $\text{TiO}_2$ -NPs was quantified using TEM-EDS analysis at different TEM spots.

The detailed analyses for texture properties using  $N_2$  adsorption–desorption isotherms, percentage of carbon and sulphur contents using CHNS analysis, as well as the percentage of sulphur using TEM-EDS for prepared  $\text{TiO}_2/\text{PrSO}_3\text{H}$  nano-catalyst, are summarised in Table 1. It was found that the loading of 1.41% of carbon and 0.28% of sulphur from  $\text{PrSO}_3\text{H}$  groups on the surface of  $\text{TiO}_2$  NPs was accompanied by a small decrease of the BET surface area with an increase of the pore volumes and sizes.

The surface chemistry of the  $\text{TiO}_2$  and  $\text{TiO}_2/\text{PrSO}_3\text{H}$  nano-catalysts was investigated by X-ray photoelectron spectroscopy (XPS) as shown in Fig. 8. The XPS analysis provides valuable insight into the surface compositions and bonding environments for both nano-catalysts. The detailed high resolution XPS of the O 1s, S 2p, C 1s, and Ti 2p peaks for  $\text{TiO}_2/\text{PrSO}_3\text{H}$  are presented in Fig. 9. The O 1s core level spectrum (Fig. 9a) was de-convoluted into three Gaussian peaks centred at 530.4, 31.75 and 533 eV indicating the presence of  $\text{Ti=O}$ ,  $\text{S=O}$  and  $\text{S-O/C-O}$ , respectively. However, it was

very difficult to distinguish between the contribution of the binding energy (BE) of the O 1s core-level for O-C and O-S bonds because both of species fell in the same energy regions [53]. The S 2p spectra (Fig. 9b) were fitted with three Gaussian peaks centred at 164.4, 166.3 and 167.4 eV assigned to the S-C, S=O and S-O, respectively, supporting the presence of  $\text{PrSO}_3\text{H}$  groups on the surface [53].

Moreover, the high resolution C 1s XPS spectra (Fig. 9c) included two Gaussian peaks centred at 285.1 and 286.4 eV which can reasonably be assigned to the C-C and C-S/C-O, respectively, in the  $\text{PrSO}_3\text{H}$  groups [54]. The above findings indicate the surface of  $\text{TiO}_2$ -NPs has been successfully functionalised with  $\text{PrSO}_3\text{H}$  groups. Fig. 9d depicts the  $\text{Ti } 2p_{1/2}$ – $\text{Ti } 2p_{3/2}$  spin-orbital splitting at 464.4 and 458.7 eV, respectively, with a BE = 5.74 eV confirming the oxidation state of Ti in the as-prepared  $\text{TiO}_2/\text{PrSO}_3\text{H}$  is IV [55–57]. The surface atomic ratios of Ti:O and S:C were determined from the XPS data and found to be 1:6.64 and 1:4.63, respectively. In fact, these ratios theoretically supposed to be 1:6 and 1:3 for Ti:O

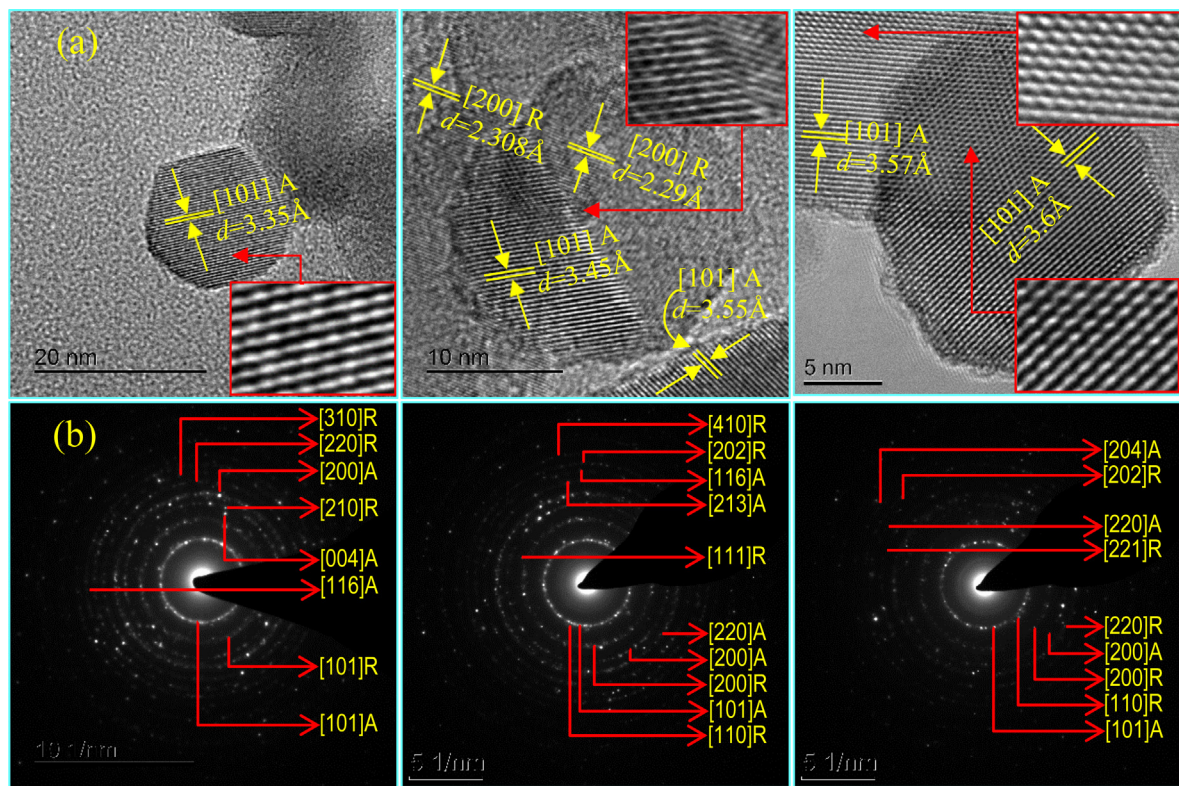


**Fig. 5.** (a) High resolution TEM (HRTEM) micrograph images and (b) selected area electron diffraction (SAED) patterns for  $\text{TiO}_2/\text{PrSO}_3\text{H}$  nano-catalyst.

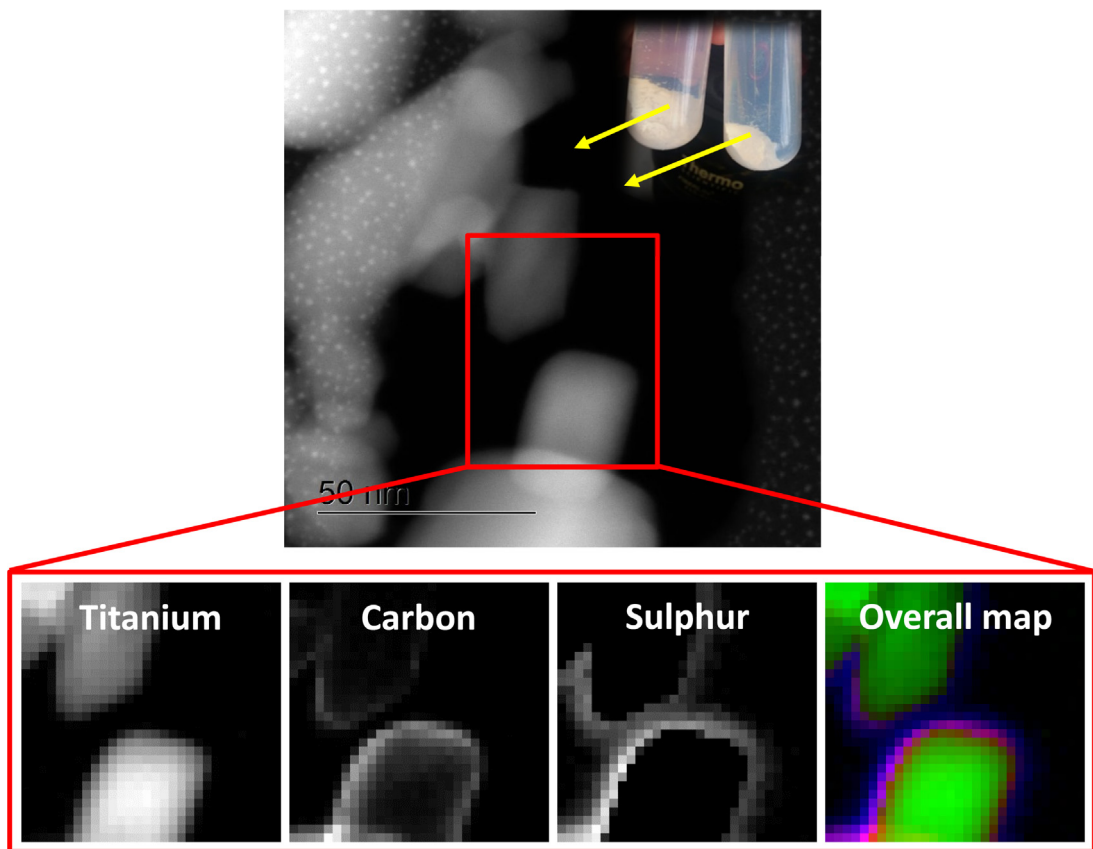


**Fig. 6.** STEM image with EELS-mapping of synthesised  $\text{TiO}_2/\text{PrSO}_3\text{H}$  nano-catalyst obtained from Titan at 300 kV illustrating the 2D elemental mapping with high quality overall map of  $\text{TiO}_2/\text{PrSO}_3\text{H}$  particles with the distribution of individual elements (Titanium in green, Carbon in violet, and Sulphur in blue). (For interpretation of the references to colour in this figure legend, the reader is referred to the web version of this article.)

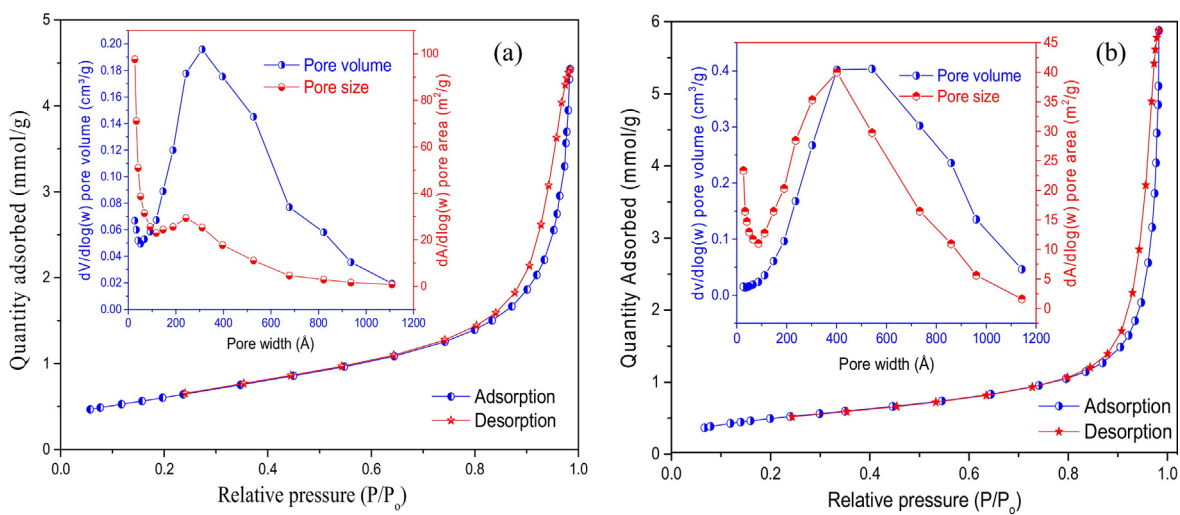


Fig. 7. N<sub>2</sub> adsorption–desorption isotherms and total pore volumes with mean pore sizes (inset) for (a) TiO<sub>2</sub> NPs and (b) synthesised TiO<sub>2</sub>/PrSO<sub>3</sub>H nano-catalysts.

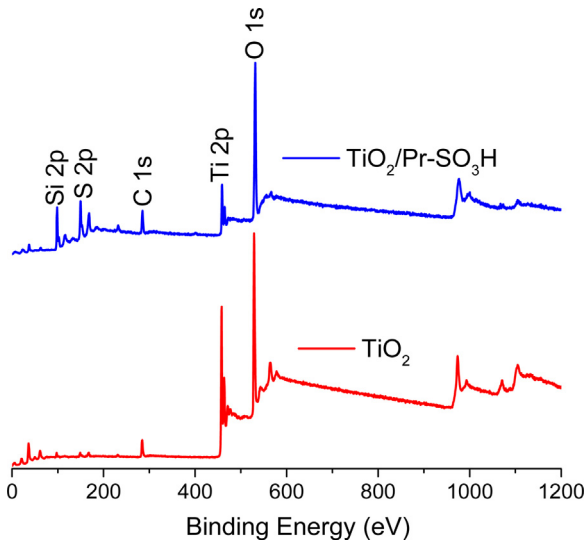


Fig. 8. XPS survey scan of TiO<sub>2</sub> NPs and synthesised TiO<sub>2</sub>/PrSO<sub>3</sub>H nano-catalysts.

and S:C, respectively. Therefore, there was an overall increase in both ratios presumably due to surface contamination of the nano-catalyst with CO<sub>x</sub> and/or H<sub>2</sub>O in the atmosphere during sample preparation for analysis. This result confirms an earlier investigation with the FT-IR spectrum for TiO<sub>2</sub>/PrSO<sub>3</sub>H nano-catalyst. In addition, the percentage of sulphur to carbon atomic ratios using XPS quantitative analysis in TiO<sub>2</sub>/PrSO<sub>3</sub>H nano-catalyst was 0.22. This is in agreements with the results obtained by CHNS analysis. In the case of TiO<sub>2</sub> NPs, the detailed high resolution XPS analysis demonstrated in our previous work [4].

Thermal stability analysis gave insights on the species evolved upon heating of the nano-catalyst that was prepared via surface grafting (PrSO<sub>3</sub>H). Fig. 10a shows the weight loss of TiO<sub>2</sub>/PrSO<sub>3</sub>H and initial TiO<sub>2</sub> NPs as determined by thermogravimetric analysis (TGA) under N<sub>2</sub> purge gas. There was a negligible weight loss from 25 to 120 °C for both samples assigned to desorption of H<sub>2</sub>O/CO<sub>x</sub> molecules from the surface of TiO<sub>2</sub>. In the case of initial TiO<sub>2</sub> NPs, there was no further mass loss up to 900 °C. In contrast, there was a gradual weight loss of about 2% from TiO<sub>2</sub>/PrSO<sub>3</sub>H at 210 to 500 °C; afterwards there was no further weight loss up to 900 °C. This is due to the thermal decomposition of PrSO<sub>3</sub>H species on the surface of TiO<sub>2</sub> NPs. This result agrees with results of the CHNS

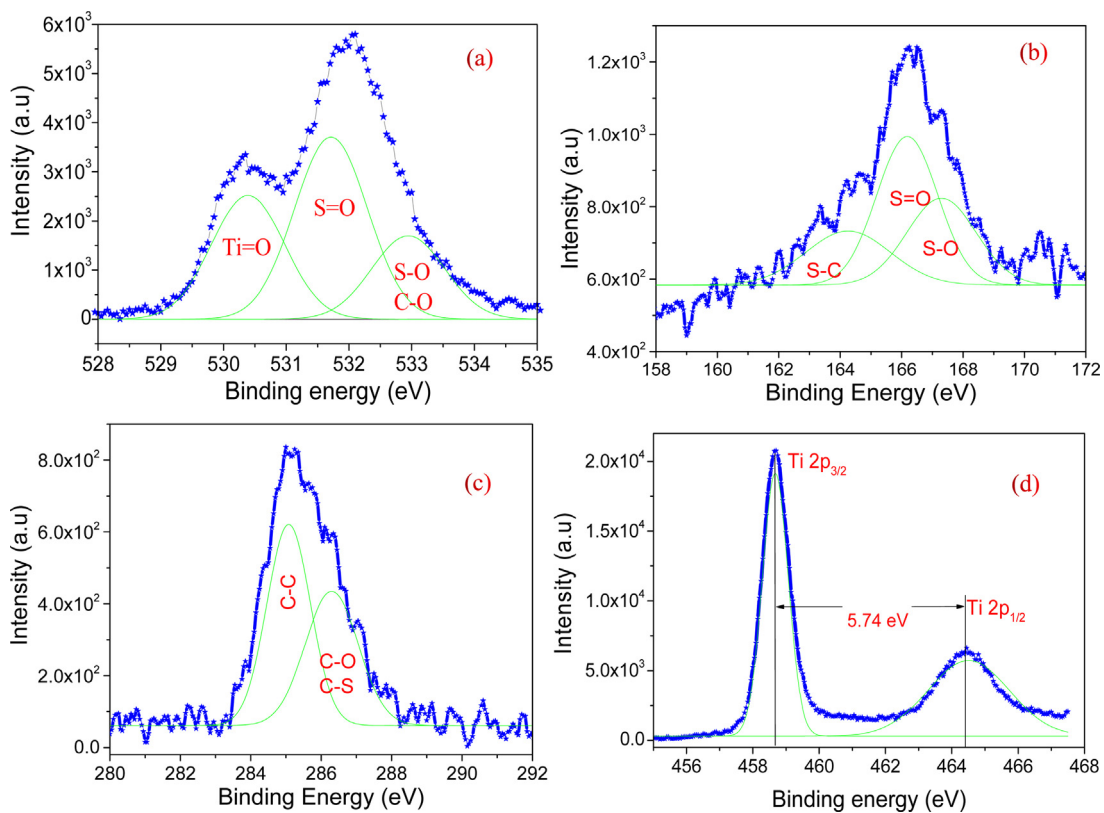
elemental analysis and is in accordance with the FT-IR results. It must be noted also from the DSC results (see Fig. 10b) that there is only one sharp distinct endothermic peak observed at 210 °C with enthalpy of -60 mJ corresponding to the decomposition of PrSO<sub>3</sub>H groups on the surface of TiO<sub>2</sub> NPs. This is further evidence that the surface of TiO<sub>2</sub> NPs was successfully functionalised with PrO<sub>3</sub>H groups.

Fig. 11 illustrates that the surface grafting of TiO<sub>2</sub> with PrSO<sub>3</sub>H groups resulted in the position shift of all diffraction peaks to a bit higher 2θ angles by 0.2° indicating the decrease of the unit-cell sizes. Moreover, a reduction of intensity in all reflections is observed for TiO<sub>2</sub>/PrSO<sub>3</sub>H as compared with the initial TiO<sub>2</sub> NPs precursor. Furthermore, the position of the main diffraction peaks with 100% intensity of initial TiO<sub>2</sub> NPs were observed at 2θ value of 25.3° corresponding to the [101] for 81.6% of tetragonal anatase phase structure (JCPDS-ICDD: 04-014-5762) whilst the peak at 2θ value of 27.43° assigned to the [110] for 18.4% of tetragonal rutile phase structure (JCPDS-ICDD: 01-072-41815). In the case of TiO<sub>2</sub>/PrSO<sub>3</sub>H nano-catalyst, the XRD patterns matched all the diffraction peaks with tetragonal anatase phase (JCPDS-ICDD: 01-084-1286) and tetragonal rutile phase (JCPDS-ICDD: 01-072-4817).

However, no characteristic extra peak was observed for the PrSO<sub>3</sub>H groups, which suggested that these groups were only grafted on the surface of TiO<sub>2</sub> NPs, rather than impregnating the main crystallographic structure as expected. The detailed interlayer spacing values and calculated crystallite sizes of the [101] peak for anatase and [110] peak for rutile from the initial TiO<sub>2</sub> NPs and PrSO<sub>3</sub>H surface functionalised TiO<sub>2</sub> NPs are summarised in Table 2.

### 3.2. Catalytic performance

The catalytic activity of TiO<sub>2</sub>/PrSO<sub>3</sub>H nano-catalyst for simultaneous esterification and transesterification of UCO to produce biodiesel fuel was investigated. The effect of different reaction times, catalyst loadings, mole ratios of methanol to oil, and reaction temperatures on the percentage of FAME yields were studied and the results are presented in Fig. 12. The reaction time of esterification/transesterification was varied between ½ and 9 h whilst other process parameters were kept constant at 1 wt% of TiO<sub>2</sub>/PrSO<sub>3</sub>H nano-catalyst to UCO feedstock, 6:1 methanol to oil mole ratio, 65 °C reaction temperature, 600 RPM agitation rate, 0.14% moisture, and <2.0% of FFA content in raw material (UCO). It was found that the initial (trans)esterification reaction rate was very low, as shown in Fig. 12a. This could possibly be due to the immiscibility



**Fig. 9.** XPS spectra showing the chemical environments of (a) O 1s, (b) S 2p, (c) C 1s, and (d) the de-convolution of Ti 2p peaks in  $\text{TiO}_2/\text{PrSO}_3\text{H}$  nano-catalyst.

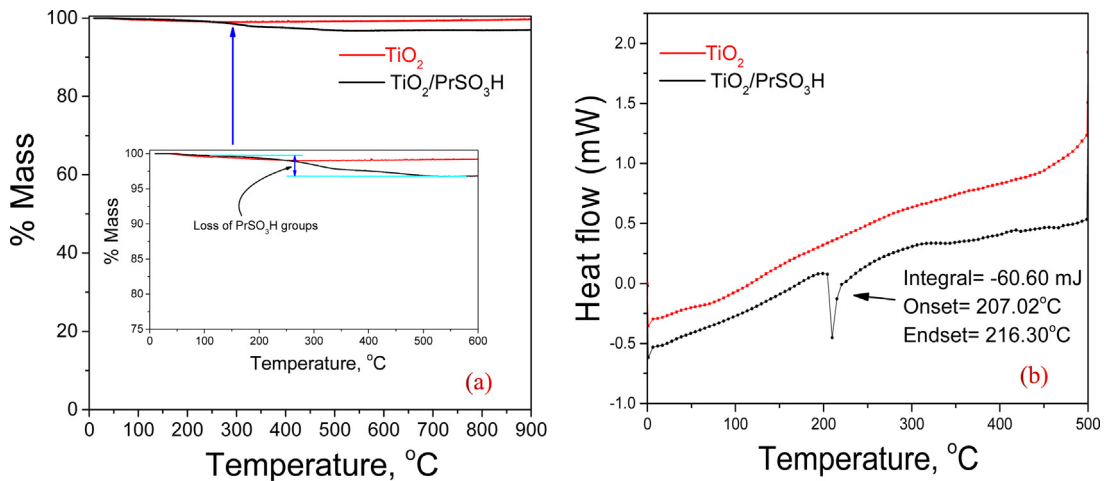


**Fig. 10.** TGA (a) and DSC (b) profiles for  $\text{TiO}_2$  and  $\text{TiO}_2/\text{PrSO}_3\text{H}$  nano-catalysts.

**Table 2**

Comparison of  $d$ -spacing and crystallite sizes of  $\text{TiO}_2$  and  $\text{TiO}_2/\text{PrSO}_3\text{H}$ .

Sample	XRD peak	$^{\circ}2\theta$	FWHM	$d$ -spacing, Å	$D^a$ , nm
$\text{TiO}_2$	[101] Anatase	25.30	0.39	3.52	20.87
	[110] Rutile	27.43	3.26	3.25	2.51
$\text{TiO}_2/\text{PrSO}_3\text{H}$	[101] Anatase	25.47	0.41	3.49	19.86
	[110] Rutile	27.52	3.26	3.24	2.51

<sup>a</sup> D: The crystallite size of the 100% relative intensities XRD main peaks for anatase and rutile phases in nano-catalysts were estimated using Debye–Scherrer's formula [4].

of reactants (solid–liquid–liquid phases)/the initial mass transfer limitations. The FAME yield further increased but was still lower than 10% FAME yield when the experiment was run for a longer time (9 h). This is because of the better miscibility of reactants (solid acid

nano-catalyst, methanol and UCO) with the time and increasing of mass transfer. The results of different catalyst to oil loadings on the FAME yield, however, shows the yield of FAME was almost doubled (see Fig. 12b) when the (trans)esterification process was set

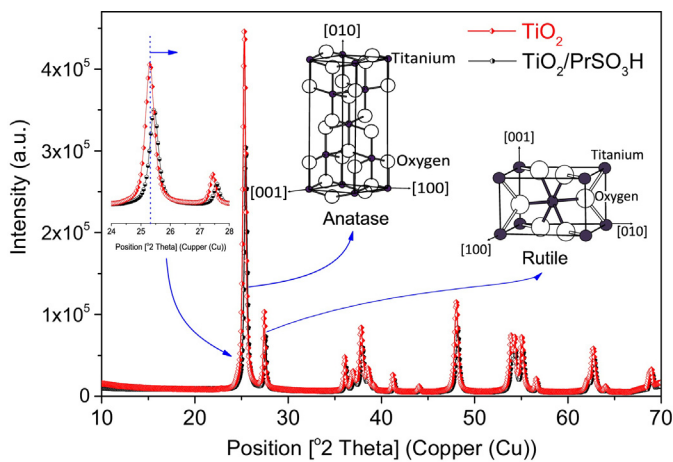


**Fig. 11.** Powder XRD profiles for  $\text{TiO}_2$  and  $\text{TiO}_2/\text{PrSO}_3\text{H}$  nano-catalysts at RT.

at 9 h of reaction time, 2 wt% of nanocatalyst to UCO, 6:1 methanol to oil mole ratio, 65 °C reaction temperature, 600 RPM of agitation rate, 0.14% moisture and <2.0% of FFA in raw material. This was attributed to the fact that the number of active sites were increasing with an increase in the catalyst concentration in the reaction system requiring a shorter time to reach the equilibrium [58]. Furthermore, the yield of FAME further increased from 14.92% to 38.7% with an increase in the nano-catalyst loading from 2 to 4.5 wt% of UCO. Increasing the catalyst concentrations will lead to an increase in the number of active sites (proton,  $-\text{SO}_3\text{H}$ , concentration in the interface), which enhanced selectivity towards the FAME product [59].

A maximum conversion of FFA/triglycerides (TG) into FAME is required in simultaneous esterification and transesterification reactions to obtain the highest yield of FAME in order to satisfy the EU and ASTM standards for obtained biodiesel fuel. In theory, the stoichiometric ratio for transesterification reaction requires three moles of methanol per mole of TG to obtain three moles of FAME and one mole of glycerol whilst this ratio is one to one for esterification reaction [60]. However, transesterification reaction practically needs an excess amount of methanol in order to get a complete conversion. In order to drive the reaction towards the highest FAME yield [61], various mole ratios of methanol to UCO were used [see Fig. 12c] under the aforementioned reaction conditions. It can be noted that the highest FAME yield of 98.1% was obtained when the mole ratio of methanol to UCO was steadily increased to 15:1 whilst the other parameters were fixed as most probably to a higher molar ratio of methanol to UCO leads to an increase of miscibility of reactants which shift the equilibrium to the product side and increase the probability of a methanol nucleophilic attack on the carbonyl/carboxylic acid functional groups in the FFA/TG. However, a further increase in mole ratio of methanol to oil leads to a slight reduction in the FAME yield [58,62], presumably as glycerol and FAME solubility in excess methanol can help to derive the reverse side of transesterification reaction [10].

The rate of esterification/transesterification reactions are strongly dependent on the process temperature. The effect of temperature on the FAME yield, whilst other parameters were set at 9 h reaction time, 4.5 wt% of  $\text{TiO}_2/\text{PrSO}_3\text{H}$  to UCO, 15:1 molar ratio of methanol to UCO, 600 RPM agitation rate, 0.14% moisture content, and <2% of FFA content in UCO raw material, is shown in Fig. 12d. It can be noted that the increase of reaction temperature from 25 to 60 °C led to smooth increase in the rate of the (trans)esterification

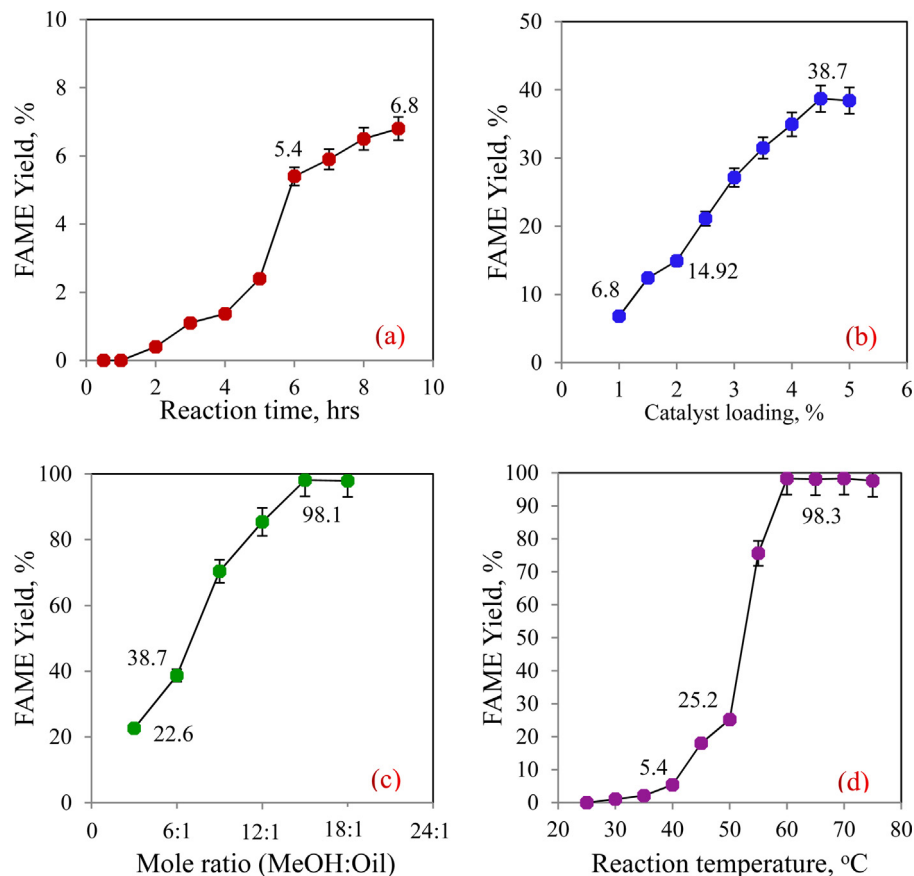


**Fig. 12.** The effects of (a) reaction time, (b)  $\text{TiO}_2/\text{PrSO}_3\text{H}$  nano-catalyst loading to UCO, (c) mole ratio of methanol to UCO, and (d) reaction temperature on the percentage of FAME yield.

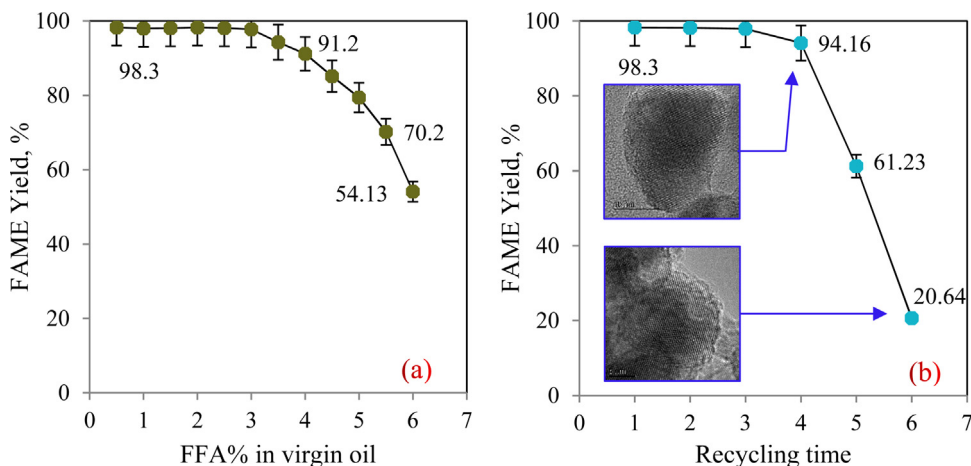


Fig. 13. The effect of different concentration oleic acid addition in virgin oil (a) and reusability of  $\text{TiO}_2/\text{PrSO}_3\text{H}$  nano-catalyst (b) on the percentage of FAME yield.

process to reach 98.3% FAME yield. The reason for obtaining a high FAME yield at a higher temperature can be explained by the fact that the higher reaction temperature accelerates (1) the movement of molecules in reactants, (2) solubility of TG in methanol, (3) diffusion of TG molecules, as well as (4) generating more nucleophilic sites in the reaction system which results in an increase in reaction rate. This could help to initiate the activation of carboxylic/carbonyl function groups in FFA/TG by nucleophile [14]. Further studies on the reaction kinetic of the esterification/transesterification reaction using  $\text{TiO}_2/\text{PrSO}_3\text{H}$  nano-catalyst should be reported in the future publications.

### 3.3. Catalytic activity and its reusability

The catalytic activity of  $\text{TiO}_2/\text{PrSO}_3\text{H}$  nano-catalyst was assessed by the addition of different percentages of oleic acid in virgin oil because the presence of FFA in the feedstock has a great influence on the deactivation of catalysts. The addition of oleic acid in virgin oil was varied from 0.5% to 6% under determined optimum reaction conditions as reported in previous section. It can be observed from Fig. 13a, that the FAME yield was greatly reduced with an increase in the percentage of oleic acids in the virgin oil as raw material. This can be explained by the rate of esterification which was much faster than the transesterification [61] producing more water (by-product) in the reaction medium in a shorter time. The produced excess water in the reaction medium would probably deactivate the active sites of the catalyst. Likewise, the presence of a high concentration of oleic acid in the reaction medium leads to the rapid formation of ester and water (by-product). Produced water from the reaction as a by-product may drive the reverse reaction to re-form FFA and methanol [63,64].

The spent  $\text{TiO}_2/\text{PrSO}_3\text{H}$  nano-catalyst was recovered from the reaction products and by-products at the end of each run by using centrifuge (Megafuge 16R, UK) and then properly washed several times with 1:1 ratio of methanol to *n*-hexane in order to remove any remaining impurities (polar and non-polar components) on its surface. The recycled catalyst was later dried in an oven for 3 h at 110 °C to remove any moisture on the surface prior to being re-used under optimised process conditions to investigate its remaining activity.

It was found that  $\text{TiO}_2/\text{PrSO}_3\text{H}$  can be re-used up to four times under optimised reaction conditions, i.e. reaction temperature of 60 °C, 4.5 wt% of  $\text{TiO}_2/\text{PrSO}_3\text{H}$  nano-catalyst to UCO, molar ratios of methanol to UCO of 15:1, 600 RPM agitation rate, 0.14% moisture, <2.0% FFA, and 9 h reaction time. However, thereafter, the yield of FAME was sharply reduced to 20.64%, as shown in Fig. 13b. This

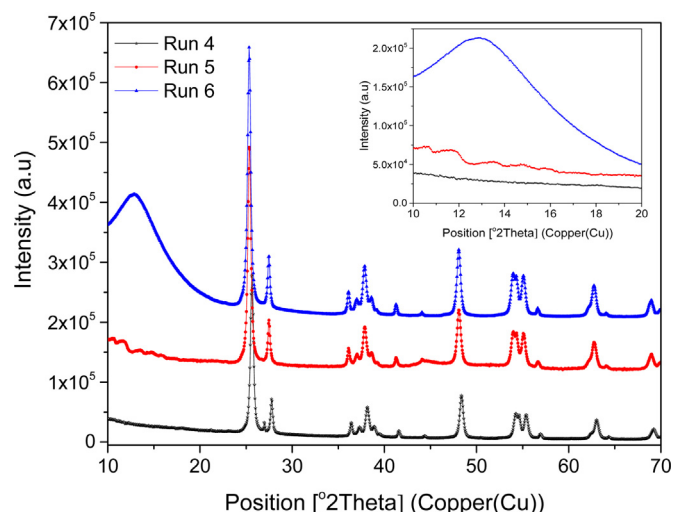


Fig. 14. Powder XRD patterns of spent  $\text{TiO}_2/\text{PrSO}_3\text{H}$  nano-catalyst for run 4 to run 6.

obvious change in the FAME yield is due to the organic or carbonaceous materials on the surface of recycled nano-catalyst causing blockage of the active sites and/or detachment (leaching) of the  $\text{PrSO}_3\text{H}$  species on the surface of  $\text{TiO}_2$ -NPs [65–68]. According to the XRD results shown in Fig. 14, there was an accumulation of organic or carbonaceous materials from the surface of the prepared mesoporous solid acid nano-catalyst after four runs. This possibly inhibited the contact between the reactants and the active sites of the nano-catalyst [10,40,44,66]. In order to fully understand the catalytic poisoning of the spent  $\text{TiO}_2/\text{PrSO}_3\text{H}$  nano-catalyst, further studies should be carried out in detail, using the XPS, temperature programmed desorption (TPD)-MS, Hammett indicator titration, TEM-EDS, and CHNS techniques.

### 3.4. Biodiesel characterisations

The properties of obtained biodiesel are mainly dependent on the FAME compositions [17]. Therefore, off-line GC-MS was used to analyse the final product in order to quantify FAME content of synthesised biodiesel using  $\text{TiO}_2/\text{PrSO}_3\text{H}$  solid acid nano-catalyst. The FAME compositions for obtained biodiesel are listed in Table 3.

It was found from Table 3 that the major FAMEs are palmitic acid methyl ester, stearic acid methyl ester, oleic acid methyl ester, linoleic acid methyl ester, linolenic acid methyl ester, and gadoleic

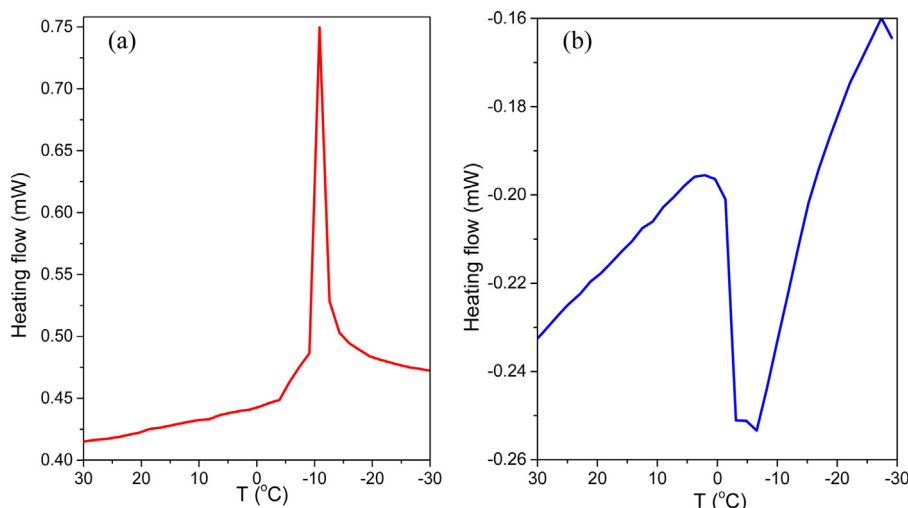


**Fig. 15.** The DSC (a) cooling and (b) heating curves for obtained biodiesel.

**Table 3**

FAME profiles for as-prepared biodiesel from UCO.

Name	% FAME
Myristic acid methyl ester	C <sub>14:0</sub> 0.07
Palmitic acid methyl ester	C <sub>16:0</sub> 7.86
Palmitoleic acid methyl ester	C <sub>16:1</sub> 0.01
Stearic acid methyl ester	C <sub>18:0</sub> 3.08
Oleic acid methyl ester	C <sub>18:1</sub> 56.19
Linoleic acid methyl ester	C <sub>18:2</sub> 26.74
Linolenic acid methyl ester	C <sub>18:3</sub> 3.30
Arachidic acid methyl ester	C <sub>20:0</sub> 0.00
Gadoleic acid methyl ester	C <sub>20:1</sub> 1.32
Eicosadienoic acid methyl ester	C <sub>21:0</sub> 0.10
Behenic acid methyl ester	C <sub>22:0</sub> 0.43
Erucic acid methyl ester	C <sub>22:1</sub> 0.64
Lignoceric acid methyl ester	C <sub>24:0</sub> 0.12
Nervonic acid methyl ester	C <sub>24:1</sub> 0.14

acid methyl ester. The quality of final biodiesel fuel obtained under optimum reaction conditions are summarised in **Table 4**. The fuel properties of obtained biodiesel fuel were evaluated and the results revealed that the quality of produced biodiesel from the current study fulfilled ASTM and EU standards for biodiesel fuel quality control.

The cloud point is the temperature at which a cloud or few crystals form in a biodiesel fuel caused by the first stage of crystallisation on cooling of the fuel. It is one of the most important properties of biodiesel, which influences its use in a cold environment due to the possibility of causing fuel injector problems, poor fuel atomisation, incomplete combustion, and deposit formation [17]. The DSC thermogram for as-synthesised biodiesel is shown in **Fig. 15**. It can be seen from the cooling DSC curve that there is only one sharp endothermic peak centred at -11°C with enthalpy of 67.14 mJ corresponding to the formation of crystals in biodiesel fuel. The onset temperature of crystallisation on the cooling curve

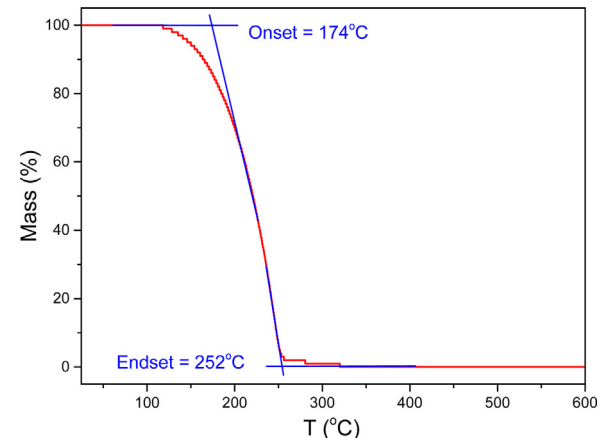


**Fig. 16.** Typical TGA thermogram of obtained biodiesel in air.

at -10.57 °C represents the cloud point temperature of prepared biodiesel. In heating DSC thermogram, a broad exothermic peak was observed between -28 and 0 °C assigned to the melting of the formed crystals.

Thermal oxidative behaviour plays a key role in the industrial application of the biodiesel fuel [69]. The TGA thermogram for prepared biodiesel with onset and endset temperatures are shown in **Fig. 16**. The onset temperature (174 °C) represent the biodiesel sample starting to decompose whilst the endset temperature (252 °C) corresponds to the completely burnt off biodiesel sample. These results indicate that the synthesised biodiesel was thermally stable in atmosphere.

**Table 4**

Properties of UCO and obtained biodiesel over TiO<sub>2</sub>/PrSO<sub>3</sub>H nano-catalyst.

Property	Unit	Limits		UCO	Synthesised biodiesel
		ASTM D6751	EN14214		
Flash point	°C	93 min	101 min	289	171
Kinematic viscosity	mm <sup>2</sup> /s	1.9–6.0	3.5–5.0	32.91	4.8
Acid number	mgKOH/g	0.8 max	0.5 max	4.04	0.41
FFA	mass%	–	–	2.034	0.21
Density at 15 °C	Kg/m <sup>3</sup>	–	860–900	921	898.1
FAME content	% mass	–	96.5 min	0.00	98.3

**Table 5**

A mild process conditions for the production of biodiesel in the simultaneous esterification and transesterification from the current work compared to the reported solid acid catalysts.

	Current study	Melero et al. [10]	Fu et al. [70]	Feyzi et al. [71]
Oil/fat feedstock	UCO/Oleic acid	Crude palm oil	Rapeseed oil/Oleic acid	Sunflower oil
Methanol to oil ratio	15:1	20:1	10:1	12:1
Type of catalyst	TiO <sub>2</sub> /PrSO <sub>3</sub> H	SBA-15-PrSO <sub>3</sub> H	β-Cyclodextrin-SO <sub>3</sub> H	CsH <sub>3</sub> PW <sub>12</sub> O <sub>40</sub> /Fe-SiO <sub>2</sub>
Amount of catalyst%	4.5	6	5.0	3
Agitation speed, RPM	600	Not reported	500	500
Time, h	9	4	12	4
Temperature, °C	60	140	60–85	60
FAME yield %	98.3	95	90.82	81
BET surface area, m <sup>2</sup> g <sup>-1</sup>	38.59	666	38.2	237.5
Mean pore size Å	245.46	82	—	173.4
Average particle size, nm	23.1	Not reported	1000	38–42
Catalyst recycled	4	2	6	Not reported

### 3.5. Discussion

A novel TiO<sub>2</sub>/PrSO<sub>3</sub>H nano-catalyst was prepared through grafting of TiO<sub>2</sub>-NPs with 1,3-propane sultone in dry toluene under reflux at 120 °C for 72 h. The application of such material as solid acid nano-catalyst is reported for the first time for biodiesel production from UCO. The synthesised solid acid nano-catalyst shows a remarkable catalytic activity for simultaneous esterification and transesterification of cheap feedstocks, probably due to the catalytic activity of such material according to its surface property (–SO<sub>3</sub>H). It is important to mention that loading of higher density hydrophilic functional groups (–SO<sub>3</sub>H) onto the surface of TiO<sub>2</sub> NPs may lead to an improvement in the hydrophilicity of TiO<sub>2</sub> NPs support and increase the accessibility of raw material (FFAs, triglycerides and methanol) in the simultaneous esterification and transesterification processes to the –SO<sub>3</sub>H groups. Therefore, more investigations could be carried out in future on the effect of different TiO<sub>2</sub> phases (anatase, rutile and brookite) with different loadings of PrSO<sub>3</sub>H species and the surface acidity/strength of TiO<sub>2</sub>/PrSO<sub>3</sub>H for the catalytic performance. Such future studies could fully utilise the potential of such nano-catalyst on the FAME yield produced from simultaneous esterification and transesterification of UCO. The prepared solid acid nano-catalyst was found to esterify FFA in cheap raw materials to FAME in parallel with transesterification of TG without formation of soaps. The nano-catalyst was also found to be a non-hazardous material compared to conventional homogenous acids and it can be used in four consecutive (trans)esterification cycles with no appreciable loss in catalytic activity, which may satisfy the principle of green chemistry. Table 5 summarises the comparison of the optimised process condition results for biodiesel production from UCO/oleic acid using solid acid catalyst in the present study with other reported solid acid catalysts in the literature.

### 4. Conclusions

Mesoporous TiO<sub>2</sub>/PrSO<sub>3</sub>H solid acid nano-catalyst with an average particle size of around 23.1 nm has been successfully synthesised as a novel inorganic–organic hybrid heterogeneous nano-catalyst from TiO<sub>2</sub> NPs and 1,3-propyl sulfonic acid for simultaneous esterification and transesterification of UCO containing FFA. STEM EELs-maps shows that the PrSO<sub>3</sub>H groups decorate the surface of TiO<sub>2</sub> NPs layer-by-layer. N<sub>2</sub> adsorption–desorption isotherms result demonstrated that surface modification reduced the surface area of TiO<sub>2</sub> NPs by 5% with an increase in the mean pore size and total pore volume. The XPS confirmed that the PrSO<sub>3</sub>H functional groups attached to the surface of TiO<sub>2</sub> NPs. TiO<sub>2</sub>/PrSO<sub>3</sub>H nano-catalyst performance showed promising results for catalytic

simultaneous esterification and transesterification of cheap raw materials for biodiesel production. The enhanced catalytic performance mainly relates to the loading of propyl sulfonic acid groups on the surface of TiO<sub>2</sub> NPs.

### Acknowledgement

The authors would like to thank Professor Karen Wilson (the European Bioenergy Research Institute, EBRI) for her highly valuable comments and discussion for this study. We are also thankful to Dr Adrian Cunliffe, Dr Mike Ward and Dr Faye Esat for their technical assistance.

### References

- [1] J. Shen, Y. Zhu, X. Yang, C. Li, Magnetic composite microspheres with exposed {001} faceted TiO<sub>2</sub> shells: a highly active and selective visible-light photocatalyst, *Journal of Materials Chemistry* 22 (26) (2012) 13341–13347.
- [2] M. Rehan, X. Lai, G.M. Kale, Hydrothermal synthesis of titanium dioxide nanoparticles studied employing *in situ* energy dispersive X-ray diffraction, *CrystEngComm* 13 (11) (2011) 3725–3732.
- [3] A. Patoursa, D.I. Kondarides, X.E. Verykios, Enhancement of photoinduced hydrogen production from irradiated Pt/TiO<sub>2</sub> suspensions with simultaneous degradation of azo-dyes, *Applied Catalysis B: Environmental* 64 (3) (2006) 171–179.
- [4] J. Gardy, A. Hassanpour, X. Lai, M.H. Ahmed, Synthesis of Ti(SO<sub>4</sub>)O solid acid nano-catalyst and its application for biodiesel production from used cooking oil, *Applied Catalysis A: General* 527 (2016) 81–95.
- [5] M.H. Ahmed, J.A. Byrne, T.E. Keyes, Investigation of the inhibitory effects of TiO<sub>2</sub> on the β-amyloid peptide aggregation, *Materials Science and Engineering C* 39 (2014) 227–234.
- [6] K. Bourikas, M. Styliadi, D.I. Kondarides, X.E. Verykios, Adsorption of acid orange 7 on the surface of titanium dioxide, *Langmuir* 21 (20) (2005) 9222–9230.
- [7] D.A. Hanaor, C.C. Sorrell, Review of the anatase to rutile phase transformation, *Journal of Materials Science* 46 (4) (2011) 855–874.
- [8] S. Kang, J. Ye, J. Chang, Recent advances in carbon-based sulfonated catalyst: preparation and application, *International Review of Chemical Engineering (IRECHE)* 5 (2) (2013) 133–144.
- [9] A. Patel, V. Brahmkhatri, Kinetic study of oleic acid esterification over 12-tungstophosphoric acid catalyst anchored to different mesoporous silica supports, *Fuel Processing Technology* 113 (2013) 141–149.
- [10] J.A. Melero, L.F. Bautista, G. Morales, J. Iglesias, R. Sánchez-Vázquez, Biodiesel production from crude palm oil using sulfonic acid-modified mesostructured catalysts, *Chemical Engineering Journal* 161 (3) (2010) 323–331.
- [11] P. Toh-Ae, B. Junhasavasdikul, N. Lopattananon, K. Sahakaro, Surface modification of TiO<sub>2</sub> nanoparticles by grafting with silane coupling agent, *Advanced Materials Research* 844 (2014) 276–279.
- [12] J. Zhao, M. Milanova, M.M. Warmoeskerken, V. Dutschk, Surface modification of TiO<sub>2</sub> nanoparticles with silane coupling agents, *Colloids and Surfaces A: Physicochemical and Engineering Aspects* 413 (2012) 273–279.
- [13] T. Radoman, J. Džunuzović, K. Trifković, T. Palija, A. Marinković, B. Bugarski, E. Džunuzović, Effect of surface modified TiO<sub>2</sub> nanoparticles on thermal, barrier and mechanical properties of long oil alkyl resin-based coatings, *Express Polymer Letters* 9 (10) (2015).
- [14] Q. Shu, J. Gao, Z. Nawaz, Y. Liao, D. Wang, J. Wang, Synthesis of biodiesel from waste vegetable oil with large amounts of free fatty acids using a carbon-based solid acid catalyst, *Applied Energy* 87 (8) (2010) 2589–2596.

- [15] A.F. Lee, K. Wilson, Recent developments in heterogeneous catalysis for the sustainable production of biodiesel, *Catalysis Today* 242 (2015) 3–18.
- [16] F.H. Alhassan, U. Rashid, Y. Taufiq-Yap, Synthesis of waste cooking oil-based biodiesel via effectual recyclable bi-functional  $\text{Fe}_2\text{O}_3\text{-MnO-SO}_4^{2-}/\text{ZrO}_2$  nanoparticle solid catalyst, *Fuel* 142 (2015) 38–45.
- [17] J. Gardy, A. Hassannour, X. Lai, A. Cunliffe, M. Rehan, The influence of blending process on the quality of rapeseed oil-used cooking oil biodiesels, *International Scientific Journal Environmental Sciences* 3 (2014) 233–240.
- [18] A. Nizami, O. Ouda, M. Rehan, A. El-Maghraby, J. Gardy, A. Hassannour, S. Kumar, I. Ismail, The potential of Saudi Arabian natural zeolites in energy recovery technologies, *Energy* 108 (2016) 162–171.
- [19] H. Wang, J. Covarrubias, H. Prock, X. Wu, D. Wang, S.H. Bossmann, Acid-functionalized magnetic nanoparticle as heterogeneous catalysts for biodiesel synthesis, *The Journal of Physical Chemistry C* 119 (46) (2015) 26020–26028.
- [20] A.E. Atabani, A.S. Silitonga, I.A. Badruddin, T. Mahlia, H. Masjuki, S. Mekhilef, A comprehensive review on biodiesel as an alternative energy resource and its characteristics, *Renewable and Sustainable Energy Reviews* 16 (4) (2012) 2070–2093.
- [21] Y.M. Sani, W.M.A.W. Daud, A.A. Aziz, Activity of solid acid catalysts for biodiesel production: a critical review, *Applied Catalysis A: General* 470 (2014) 140–161.
- [22] A. Refaat, Biodiesel production using solid metal oxide catalysts, *International Journal of Environmental Science & Technology* 8 (1) (2011) 203–221.
- [23] S.-w. Gong, J. Lu, H.-h. Wang, L.-j. Liu, Q. Zhang, Biodiesel production via esterification of oleic acid catalyzed by picolinic acid modified 12-tungstophosphoric acid, *Applied Energy* 134 (2014) 283–289.
- [24] A.F. Lee, Catalysing sustainable fuel and chemical synthesis, *Applied Petrochemical Research* 4 (1) (2014) 11–31.
- [25] J.A. Melero, J. Iglesias, G. Morales, Heterogeneous acid catalysts for biodiesel production: current status and future challenges, *Green Chemistry* 11 (9) (2009) 1285–1308.
- [26] S. Kango, S. Kalia, A. Celli, J. Njuguna, Y. Habibi, R. Kumar, Surface modification of inorganic nanoparticles for development of organic–inorganic nanocomposites—a review, *Progress in Polymer Science* 38 (8) (2013) 1232–1261.
- [27] S. Laurent, D. Forge, M. Port, A. Roch, C. Robic, L. Vander Elst, R.N. Muller, Magnetic iron oxide nanoparticles: synthesis, stabilization, vectorization, physicochemical characterizations, and biological applications, *Chemical Reviews* 108 (6) (2008) 2064–2110.
- [28] S. Atghia, S.S. Beigbaghlo, Nanocrystalline titania-based sulfonic acid ( $\text{TiO}_2\text{-Pr-SO}_3\text{H}$ ) as a new, highly efficient and recyclable solid acid catalyst for the N-Boc protection of amines at room temperature, *Journal of Organometallic Chemistry* 745 (2013) 42–49.
- [29] X. Mo, D.E. López, K. Suwannakarn, Y. Liu, E. Lotero, J.G. Goodwin, C. Lu, Activation and deactivation characteristics of sulfonated carbon catalysts, *Journal of Catalysis* 254 (2) (2008) 332–338.
- [30] B.K. Ahn, H. Wang, S. Robinson, T.B. Shrestha, D.L. Troyer, S.H. Bossmann, X.S. Sun, Ring opening of epoxidized methyl oleate using a novel acid-functionalized iron nanoparticle catalyst, *Green Chemistry* 14 (1) (2012) 136–142.
- [31] J.A. Melero, L.F. Bautista, J. Iglesias, G. Morales, R. Sánchez-Vázquez, I. Suárez-Marcos, Biodiesel production over arenesulfonic acid-modified mesostructured catalysts: optimization of reaction parameters using response surface methodology, *Topics in Catalysis* 53 (11–12) (2010) 795–804.
- [32] W.L. Li, S.B. Tian, F. Zhu, Sulfonic acid functionalized nano- $\gamma\text{-Al}_2\text{O}_3$ : a new, efficient, and reusable catalyst for synthesis of 3-substituted-2h-1, 4-benzothiazines, *The Scientific World Journal* (2013) 2013.
- [33] L. Yang, Y. Wang, G. Luo, Y. Dai, Functionalization of SBA-15 mesoporous silica with thiol or sulfonic acid groups under the crystallization conditions, *Microporous and Mesoporous Materials* 84 (1) (2005) 275–282.
- [34] I. Díaz, C. Márquez-Alvarez, F. Mohino, J.n. Pérez-Pariente, E. Sastré, Combined alkyl and sulfonic acid functionalization of MCM-41-type silica: part 2. Esterification of glycerol with fatty acids, *Journal of Catalysis* 193 (2) (2000) 295–302.
- [35] J.A. Melero, R. van Grieken, G. Morales, Advances in the synthesis and catalytic applications of organosulfonic-functionalized mesostructured materials, *Chemical Reviews* 106 (9) (2006) 3790–3812.
- [36] M. Alvaro, A. Corma, D. Das, V. Fornés, H. García, Nafion®-functionalized mesoporous MCM-41 silica shows high activity and selectivity for carboxylic acid esterification and Friedel–Crafts acylation reactions, *Journal of Catalysis* 231 (1) (2005) 48–55.
- [37] C. Pirez, M.T. Reche, A. Lee, J. Manayil, V. dos-Santos, K. Wilson, Hydrothermal saline promoted grafting of periodic mesoporous organic sulfonic acid silicas for sustainable FAME production, *Catalysis Letters* 145 (7) (2015) 1483–1490.
- [38] S. Sobhani, Z.P. Parizi, N. Razavi, Nano n-propylsulfonated  $\gamma\text{-Fe}_2\text{O}_3$  as magnetically recyclable heterogeneous catalyst for the efficient synthesis of  $\beta$ -phosphonomalonates, *Applied Catalysis A: General* 409 (2011) 162–166.
- [39] D. Margolese, J. Melero, S. Christiansen, B. Chmelka, G. Stucky, Direct syntheses of ordered SBA-15 mesoporous silica containing sulfonic acid groups, *Chemistry of Materials* 12 (8) (2000) 2448–2459.
- [40] D. Zuo, J. Lane, D. Culy, M. Schultz, A. Pullar, M. Waxman, Sulfonic acid functionalized mesoporous SBA-15 catalysts for biodiesel production, *Applied Catalysis B: Environmental* 129 (2013) 342–350.
- [41] I.K. Mbaraka, K.J. McGuire, B.H. Shanks, Acidic mesoporous silica for the catalytic conversion of fatty acids in beef tallow, *Industrial & Engineering Chemistry Research* 45 (9) (2006) 3022–3028.
- [42] E.I. Basaldella, M.S. Legnoverde, I. Jiménez-Morales, E. Rodríguez-Castellón, B.O. Dalla Costa, C.A. Querini, Preparation, characterization and catalytic activity towards green reactions of sulfonic functionalized SBA-15, *Adsorption* 17 (3) (2011) 631–641.
- [43] E. Lotero, J.G. Goodwin Jr., D.A. Bruce, K. Suwannakarn, Y. Liu, D.E. Lopez, The catalysis of biodiesel synthesis, *Catalysis* 19 (1) (2006) 41–83.
- [44] J.A. Melero, L.F. Bautista, J. Iglesias, G. Morales, R. Sánchez-Vázquez, K. Wilson, A.F. Lee, New insights in the deactivation of sulfonic modified SBA-15 catalysts for biodiesel production from low-grade oleaginous feedstock, *Applied Catalysis A: General* 488 (2014) 111–118.
- [45] D. Bahnemann, A. Henglein, L. Spanhel, Detection of the intermediates of colloidal  $\text{TiO}_2$ -catalysed photoreactions, *Faraday Discussions of the Chemical Society* 78 (1984) 151–163.
- [46] G.D.A. Soler-Illia, A. Louis, C. Sanchez, Synthesis and characterization of mesostructured titania-based materials through evaporation-induced self-assembly, *Chemistry of Materials* 14 (2) (2002) 750–759.
- [47] D.L. Pavia, G.M. Lampman, G.S. Kriz, J.A. Vyvyan, *Introduction to spectroscopy*, Cengage Learning, US, 2008.
- [48] R. Sirsam, G. Usmani, Preparation and characterization of sulfonic acid functionalized silica and its application for the esterification of ethanol and maleic Acid, *Journal of The Institution of Engineers (India): Series E* 97 (1) (2016) 75–80.
- [49] P. Muthirulan, C.N. Devi, M.M. Sundaram,  $\text{TiO}_2$  wrapped graphene as a high performance photocatalyst for acid orange 7 dye degradation under solar/UV light irradiations, *Ceramics International* 40 (4) (2014) 5945–5957.
- [50] A.H. Lu, E.e.L. Salabas, F. Schüth, Magnetic nanoparticles: synthesis, protection, functionalization, and application, *Angewandte Chemie International Edition* 46 (8) (2007) 1222–1244.
- [51] P. Klobes, K. Meyer, R.G. Munro, Porosity and specific surface area measurements for solid materials. Special publication 960-17, 2006, US Department of Commerce, Technology Administration, National Institute of Standards and Technology.
- [52] M.K. Lam, K.T. Lee, A.R. Mohamed, Sulfated tin oxide as solid superacid catalyst for transesterification of waste cooking oil: an optimization study, *Applied Catalysis B: Environmental* 93 (1) (2009) 134–139.
- [53] F. Barroso-Bujans, J. Piero, S. Rojas, S. Sánchez-Cortes, M. Arroyo, M. López-Manchado, Degree of functionalization of carbon nanofibers with benzenesulfonic groups in an acid medium, *Carbon* 45 (8) (2007) 1669–1678.
- [54] J. Hueso, J. Espinós, A. Caballero, J. Cotrino, A. González-Elipe, XPS investigation of the reaction of carbon with NO, O<sub>2</sub>, N<sub>2</sub> and H<sub>2</sub>O plasmas, *Carbon* 45 (1) (2007) 89–96.
- [55] J. Chastain, R.C. King, J. Moulder, *Handbook of X-Ray Photoelectron Spectroscopy: A Reference Book of Standard Spectra for Identification and Interpretation of XPS Data*, Physical Electronics Eden Prairie, MN, 1995.
- [56] L. Wu, Y. Zhou, W. Nie, L. Song, P. Chen, Synthesis of highly monodispersed teardrop-shaped core–shell  $\text{SiO}_2/\text{TiO}_2$  nanoparticles and their photocatalytic activities, *Applied Surface Science* 351 (2015) 320–326.
- [57] H.M. Yadav, S.V. Otari, V.B. Koli, S.S. Mali, C.K. Hong, S.H. Pawar, S.D. Delekar, Preparation and characterization of copper-doped anatase  $\text{TiO}_2$  nanoparticles with visible light photocatalytic antibacterial activity, *Journal of Photochemistry and Photobiology A: Chemistry* 280 (2014) 32–38.
- [58] Y. Li, S. Lian, D. Tong, R. Song, W. Yang, Y. Fan, R. Qing, C. Hu, One-step production of biodiesel from *Nannochloropsis* sp. on solid base Mg-Zr catalyst, *Applied Energy* 88 (10) (2011) 3313–3317.
- [59] Q. Shu, Q. Zhang, G. Xu, Z. Nawaz, D. Wang, J. Wang, Synthesis of biodiesel from cottonseed oil and methanol using a carbon-based solid acid catalyst, *Fuel Processing Technology* 90 (7) (2009) 1002–1008.
- [60] J. Li, X. Wang, W. Zhu, F. Cao,  $\text{Zn}_{1.2}\text{H}_{0.6}\text{PW}_{12}\text{O}_{40}$  nanotubes with double acid sites as heterogeneous catalysts for the production of biodiesel from waste cooking oil, *ChemSusChem* 2 (2) (2009) 177–183.
- [61] M.G. Kulkarni, R. Gopinath, L.C. Meher, A.K. Dalai, Solid acid catalyzed biodiesel production by simultaneous esterification and transesterification, *Green Chemistry* 8 (12) (2006) 1056–1062.
- [62] G. Teng, L. Gao, G. Xiao, H. Liu, Transesterification of soybean oil to biodiesel over heterogeneous solid base catalyst, *Energy & Fuels* 23 (9) (2009) 4630–4634.
- [63] D. Rattanaphra, A. Harvey, P. Srinophakun, Simultaneous conversion of triglyceride/free fatty acid mixtures into biodiesel using sulfated zirconia, *Topics in Catalysis* 53 (11–12) (2010) 773–782.
- [64] G. Morales, L.F. Bautista, J.A. Melero, J. Iglesias, R. Sánchez-Vázquez, Low-grade oils and fats: effect of several impurities on biodiesel production over sulfonic acid heterogeneous catalysts, *Bioresource Technology* 102 (20) (2011) 9571–9578.
- [65] W. Xie, C. Zhang, Propylsulfonic and arenesulfonic functionalized SBA-15 silica as an efficient and reusable catalyst for the acidolysis of soybean oil with medium-chain fatty acids, *Food Chemistry* 211 (2016) 74–82.
- [66] D.E. Lopez, J.G. Goodwin, D.A. Bruce, E. Lotero, Transesterification of triacetin with methanol on solid acid and base catalysts, *Applied Catalysis A: General* 295 (2) (2005) 97–105.
- [67] J. Jitputti, B. Kitiyanan, P. Rangsuvanvit, K. Bunyakiat, L. Attanatho, P. Jenvanitpanjakul, Transesterification of crude palm kernel oil and crude

- coconut oil by different solid catalysts, *Chemical Engineering Journal* 116 (1) (2006) 61–66.
- [68] X. Mo, E. Lotero, C. Lu, Y. Liu, J.G. Goodwin, A novel sulfonated carbon composite solid acid catalyst for biodiesel synthesis, *Catalysis Letters* 123 (1–2) (2008) 1–6.
- [69] Y. Xu, M.A. Hanna, Synthesis and characterization of hazelnut oil-based biodiesel, *Industrial Crops and Products* 29 (2) (2009) 473–479.
- [70] X.-b. Fu, J. Chen, X.-l. Song, Y.-m. Zhang, Y. Zhu, J. Yang, C.-w. Zhang, Biodiesel production using a carbon solid acid catalyst derived from  $\beta$ -cyclodextrin, *Journal of the American Oil Chemists' Society* 92 (4) (2015) 495–502.
- [71] M. Feyzi, L. Nourozi, M. Zakarianezhad, Preparation and characterization of magnetic  $\text{CsH}_2\text{PW}_{12}\text{O}_{40}/\text{Fe-SiO}_2$  nanocatalysts for biodiesel production, *Materials Research Bulletin* 60 (2014) 412–420.